Fate of Artificially Injected Oxygen in the Hypolimnion of a Two-Basin Lake: Amisk Lake, revisited

J. C. Toledo[1], V. Singleton[2], J. Little[2], G. Lawrence[3], C. L. Ramón[1,4], F. J. Rueda[1,5]

[1] Department of Civil Engineering, University of Granada, Spain.

[2] Department of Civil and Environmental Engineering, Virginia Tech, USA.

[3] Department of Civil Engineering, University of British Columbia, Canada.

[4] Department of Surface Waters - Research and Management, EAWAG, Kastanienbaum, Switzerland

[5] Water Research Institute, University of Granada, Spain.

Corresponding author: Jorge C. Toledo (jorget@correo.ugr.es)

Key Points:

- The role of plume-induced circulation in oxygen transport in a two-basin lake is assessed with a coupled bubble-plume and hydrodynamic model

- Large-scale plume-induced circulation was previously thought to be the main driver of inter-basin oxygen transport

- The time-averaged circulation in the channel is shown to be driven by internal waves and not the plume

Abstract

Bubble-plume diffusers are increasingly used to add dissolved oxygen (DO) to the hypolimnion of lakes and reservoirs. Bubble plumes are successful at replenishing hypolimnetic DO, but they also introduce mixing energy that induces subtle changes in the thermal structure of the reservoir, driving changes in plume behavior. To account for this complex plume-reservoir interaction, a double bubble-plume model is coupled with a three-dimensional hydrodynamic model. The coupled model is used to reassess a field-scale analysis of the bubble-plume diffuser in two-basin Amisk Lake, aiming at evaluating the relative role of bubble-induced circulation and internal-seiching in driving inter-basin transport under stratified conditions. A large-scale plume-induced circulation was previously thought to be the main driver of inter-basin oxygen transport. This interpretation was based on the attribution of the time-averaged circulation in the channel due to plume operation. However, the intrinsic complexity of the hydraulic system and the sparseness of the field data introduced large uncertainties in the previous analysis. Here, we demonstrate that the time-averaged circulation is primarily the result of wind-driven internal seiches. Oxygen exchange is shown to be controlled by the interaction between internal seiche-driven horizontal transport along the channel, and, the rate at which added oxygen reaches the layers above the sill, which is mainly controlled by plume-induced circulation. Internal-seiche driven transport through basin constrictions will vary depending on the magnitude of the wind forcing, depth of the thermocline and the channel geometry. These results highlight the importance of understanding water movement prior to introducing restoration actions in lakes.

Plain Language Summary

Dissolved oxygen bubble-plume diffusers are commonly used to alleviate low oxygen levels in deeper lakes or reservoirs during summer stratification or under ice cover. Bubble plumes induce large-scale mixing as a result of the added energy, altering the density structure of the lake, which, in turn, alters plume behavior. To simulate this complex interaction in a two-basin lake (Amisk Lake, Canada), a three-dimensional coupled bubble-plume reservoir model is used. Our goal is to revisit the attribution exercise conducted earlier by Lawrence et al. (1997), based on field data collected during a 30-day operational period in June 1991. Although plume-induced circulation was previously thought to be primarily responsible for oxygen transport between the

two basins under stratified conditions, here we demonstrate that oxygen transport across the sill is largely driven by internal-seiching and not by the plume.

1 Introduction

The persistence of low DO concentrations in the hypolimnion during summer stratification, and throughout the water column under ice cover, is a common water quality problem in eutrophic lakes. A restoration technique commonly used to alleviate problems associated with low DO conditions consists of adding pure oxygen gas to the deeper water through porous diffusers (Singleton & Little, 2006). The resulting oxygen bubbles create a gas/water mixture that rises and gains momentum due to a positive buoyancy flux. The buoyant mixture entrains water from the ambient, which increases the water flow rate and cross-sectional area but decreases the momentum. The plume rises against the vertical density gradient until the depth of maximum plume rise (DMPR) is reached, which is where the plume momentum is zero. The plume water at this depth is negatively buoyant and is expected to fall back to an equilibrium depth (ED) where the plume density equals the ambient density (McGinnis et al., 2004). Upon reaching the ED, the plume water intrudes horizontally into the far-field (Singleton & Little, 2006) leading to basin-scale motion that distributes the added oxygen in the hypolimnion. Plumes, therefore, induce large-scale hypolimnetic mixing as a result of the added energy, altering the density structure of the reservoir and establishing a feedback loop that continually changes plume behavior (McGinnis et al., 2004).

Many studies have been conducted on the hydraulics of bubble-plumes in stratified systems, but probably the first comprehensive model accounting for volumetric changes due to gas transfer as well as changing hydrostatic pressure and water temperature, was the discrete-bubble plume integral model of Wüest et al. (1992). The model was originally designed for a circular bubble-plume, but since first proposed, it has been successfully adapted to simulate diffused-bubble aeration in large vertical tanks, field-scale linear bubble-plume diffusers (Little & McGinnis, 2001; Singleton et al., 2007) and other oxygenation devices. Given the diffuser location and operating characteristics, and, the ambient density and oxygen concentrations, the model provides accurate predictions of plume dimensions and flow rates as plume water rises, but it does not simulate the fate of the resulting oxygen-enriched water. More recently, Socolofsky et al. (2008) proposed a double-plume model, in which the plume is described as consisting of a rising multiphase and buoyant inner plume surrounded by a counterflowing outer ring of denser fluid. This model explicitly accounts for the fall-back motion of the detrainment flow occurring

after the plume water reaches the DMPR, so that the equilibrium depth ED, where the plume water is detrained into the stratified water column, depends on the interaction of the fall-back (outer plume), the inner plume and the ambient water. Singleton et al. (2010) coupled the discrete bubble-plume model for a linear diffuser proposed by Singleton et al. (2007), and based on the discrete-bubble plume integral model of Wüest et al. (1992), to a widely used three-dimensional lake and reservoir model (Smith, 2006), so that the close interaction of plumes and basin-scale mixing processes could be explicitly simulated. The three-dimensional (3D) coupled bubble-plume reservoir model of Singleton et al. (2010) was successfully validated against an extensive data set collected in Spring Hollow Reservoir, Virginia, U.S.A.

Recent developments regarding plume dynamics (Socolofsky et al., 2008; Wüest et al., 1992) and plume-lake interactions (Singleton et al., 2010) have been successfully used in the analysis, design and operation of oxygenation systems (Bryant et al., 2011). These developments should be equally valuable when used to re-analyze previous work conducted on the field-scale performance of bubble-plume oxygenation systems. This reanalysis could be especially useful in complex settings with strong interactions between plume-dynamics and large-scale hydrodynamic processes, where the full potential of the most recent simulation tools can be exploited. The reexamination of earlier data sets could provide further validation of the new simulation tools, and could also be useful to enhance earlier interpretations of field data, which is usually challenging and often affected by large uncertainties, given the sparseness of the data.

The goal of this work is to reassess the previous results of Lawrence et al. (1997) on the field-scale performance of a bubble-plume oxygenation system installed in Amisk Lake, Canada, a two-basin lake where natural and plume-induced transport were shown to be in close interaction. Amisk Lake, 175 km northeast of Edmonton, Alberta, is a long (8 km) and relatively narrow (mean width 0.6 km) lake with two distinct basins (Fig. 1). The larger, south (S)-basin has a surface area of 2.3 km^2, a mean depth of 19.4 m, and a maximum depth of 60 m. The north (N)-basin has a surface area of 2.8 km^2, a mean depth of 10.8 m, and a maximum depth of 34 m (Mitchell & Prepas, 1990). The connecting channel is approximately 1000 m long and 300 m wide with a sill depth of 12 m (Fig. 1). Oxygen diffusers were installed 1 m off the sediment at the deepest site of the N-basin (N2, Fig. 1, see Prepas et al., 1997) in June 1988 and were fully operational from July 1990 until October 1993. Experimental observations collected prior to the installation of the diffusers revealed a persistent stratification during most of the year, with

mixing being incomplete during spring and fall, and a summer metalimnion extending from ca. 5 m to 10 m below the free surface in both basins (Prepas et al., 1997). Given the observed stratification patterns and the shallow depth of the channel, it was initially assumed that the transfer of oxygen into the S-basin would have been restricted. However, hypolimnetic oxygen injection increased DO concentrations in the S-basin as well as in the N-basin. Given the physical restriction to horizontal motion posed by the sill, a one-dimensional (1D) model of the lake would lead to dubious results. Hence, it is in cases such as Amisk Lake that a coupled 3D bubble-plume lake model can be most useful.

Two potential mechanisms were proposed by Lawrence et al. (1997) to explain the exchange of oxygenated water across the sill in Amisk Lake under stratified conditions (summer), when the oxygenation system was in operation. The first is diffuser-induced circulation driving the inter-basin exchange of water and oxygen (Fig. 1). The second is that wind-generated internal seiches resulted in transport of oxygen through the connecting channel, in a process called "internal seiche pumping" (van Senden & Imboden, 1989). Field data collected in 1991 during a 30-day period were analyzed by Lawrence et al. (1997) to obtain order of magnitude estimates of those two mechanisms as drivers of exchange of oxygenated water between the N- and S-basins. Their analysis consisted of interpretation of the spatially sparse experimental data set, using scaling arguments and simplified models of relevant processes, and introducing reasonable assumptions where experimental data was unavailable. This will be referred to as an "empirical analysis" from here on. Based on that empirical analysis, it was concluded that diffuser-driven currents were the dominant mechanism of exchange and could account for a large fraction of the oxygen injected into the S-basin. This conclusion was based on the existence of "a persistent, long-term average circulation" that Lawrence et al. (1997) observed at the channel between the two basins, with southward residual flows between 2 and 9 m of depth. It is within that range of depths ($\approx$ 7.5 m) and within the metalimnion that, based on the results of the model proposed by Schladow (1992) (see also Schladow & Fischer, 1995), it was assumed that the plume water would detrain and spread radially.

The case of Amisk Lake is of particular interest because two competing effects, one representing the signature of human activities (bubble plumes) and the other representing a natural process (wind-driven internal oscillations), are present and can influence the inter-basin exchange. The field data collected in Amisk Lake in July 1991 and the conclusions that arise from the empirical

analysis are particularly relevant as they have been used as an example of large-scale plume-induced circulation in lakes (Lee & Chu, 2012). Here, in light of recent developments on plume-dynamics and three-dimensional modeling, we revisit the attribution exercise conducted by Lawrence et al. (1997), reevaluating the contributions of bubble-plume induced circulation and internal-seiching as drivers of inter-basin exchange.

2 Materials and Methods

2.1 Approach

The operation of a bubble-plume oxygenation system in Amisk Lake was simulated during a period of 30 days in 1991, starting on day 181 (30 June) and finishing on day 211 (30 July). This will be referred to as the study period. A coupled 3D plume-lake model was used to assess the role of the bubble-plume as driver of the inter-basin transport of oxygenated water during the study period (details in Supporting Information). The coupled model explicitly simulates the interaction of the near-field dynamics of the oxygenation plume (represented by a 1D-integral plume model) and the far-field large-scale transport dynamics (represented by a 3D-lake model). Different scenarios were simulated to assess the relative contribution of internal seiche pumping and plume-induced circulation to inter-basin exchange of injected oxygen.

2.2 Field data

The observations used in this study for model validation and analysis are those described by Lawrence et al. (1997). A summary of the field data is included for the sake of completeness. During the study period, pure oxygen was injected, with an average volumetric flow rate of $Q_0 = 10.9 \times 10^{-3}$ m^3 s^{-1} and a total head $H = 44$ m. Meteorological data, including records of wind speed and direction, air temperature and relative humidity, and solar radiation, were collected at site S3 (Fig. 1) on a 10-min basis, starting on day 164 in 1991 and ending on day 215. The solar radiation data were missing due to instrument malfunctioning before day 188. Water temperatures were recorded at 10-min intervals using a thermistor chain deployed at site S3 with sensors located at 3, 5, 8, 10 and 12 m below the free surface. Continuous ADCP velocity observations were collected at a site near NC and averaged in time and depth to get hourly records at 1 m bin intervals, starting on day 181 and ending on day 209. Temperature and DO

concentration profiles were collected at sites S2 and N2 on days 181 and 209. The model was initialized using conditions measured on day 181 (Fig. 1). The strong temperature gradient around 5 m depth (Fig. 1) defined the thermocline and confined the injected oxygen below.

2.3 Amisk Lake model

Transport and mixing processes in Amisk Lake during the study period were simulated with a 3D lake-plume model, in which the 3D shallow-water equation model of Smith (2006) and the double-plume model of Socolofsky et al. (2008) are coupled as outlined by Singleton et al. (2010). Entrainment into the plume is simulated as a sink of mass in the 3D model. Detrainment, in turn, is represented as a source of mass which is concentrated at the equilibrium depth ED where the detrainment flow from the outer plume is neutrally buoyant (see, for example, Asaeda & Imberger, 1993). In the World Lake Database, the oxygenation system in Amisk Lake is reported as consisting of a unique diffuser of rectangular platform of 2.4 m wide and 15 m long (https://wldb.ilec.or.jp/Display/html/3445). Prepas and Burke (1997), in turn, indicated that oxygen was injected through "one (1988–1989) or two (1990–1993) diffusers placed 100 m apart and suspended 1 m above the sediments at the deepest site in North Amisk (34 m)". The areas covered by the diffusers are not reported though. Given the uncertainty in the area and distribution of the diffusers, it was assumed that the footprint of the bubble-plume in the model could be well described as having a circular-geometry with a source area of 36 m^2. Inter-basin exchange of injected oxygen in a series of preliminary simulations conducted with alternative diffuser configurations differed by less than 12%. Operational parameters of the oxygenation system (source area, volumetric flow rates and initial-bubble diameters) were taken from earlier reports (see Table 1). The values of other bubble-plume model parameters largely follow the recommendations of Socolofsky et al. (2008). With the parameter values given in Table 1, the simulated plume did not contract near the source. The initial buoyancy flux, B_0, calculated in terms of the liquid volume flux and the reduced gravity of the air-water mixture at the source, is 0.0031 m^{4}s^{-3}; the initial bubble slip velocity U_s, calculated as in Wüest et al. (1992), for the largest bubble reported is 0.22 ms^{-1}. The characteristic length scale D, proposed by Bomdardelli et al. (2007) to parameterize the behavior of the bubble plume model defined as

$$D = \frac{B_0}{4\pi\alpha^2 U_s^3} \tag{1}$$

was 9.19 m. As argued by Wang et al. (2019) the plume will have an entraining structure for $z/D < 5$. For $z = -34$ m (maximum depth at the diffuser site), the ratio $z/D = 3.7 < 5$, which indicates that, indeed, the bubble-plume created by the oxygenation system in Amisk Lake had the structure of an entraining plume.

Initial conditions for temperature and DO in the N- and S- basins were defined with the profiles collected on day 181 at sites N2 and S2, respectively (Fig. 1). The coupled 3D lake-plume model was forced using both a source of bubbles at the site of the diffusers in the N-basin (site N2), and the meteorological forcing through the air-water interface considered horizontally uniform and estimated from the observations at site S3. For the study period, and given the long hydraulic residence time of water in the lake (~8 years, Prepas et al., 1997), inflows and outflows were considered negligible. The simulation initialized with field data and forced with the most realistic information will be referred to as "reference" scenario (Table 2). The results of this simulation were first compared against the available observations for model validation (see Supporting Information). Instantaneous and time-averaged velocity records collected in the channel were well reproduced by the model. The long-term changes in stratification occurring during the study period and the synoptic and diurnal temperature fluctuations observed at site S3 were also well reproduced.

Oxygen was simulated as a passive tracer with no sources or sinks other than the plume. Hence, our results are only valid for comparison purposes, the loading rates computed from simulated oxygen concentrations representing an upper bound to the real values. The inter-basin oxygen exchange rate was estimated in all simulations by integrating in space and time the product of flow rate and dissolved oxygen concentration at the cross section at site NC.

2.4 Synthetic simulations

A series of synthetic simulations were conducted to analyze the exchange of oxygen between the two basins and to establish the dominant exchange mechanisms (Table 2). To specifically track the plume oxygen injected during the study period, simulations were conducted in which a numerical tracer was injected through the diffuser at the same loading rate as oxygen, into an initially zero concentration field. This tracer will be referred to as "injected plume-DO". The

difference between "injected plume-DO" and the DO concentrations from the reference simulations (full-DO in Table 2) will represent the "pre-existing" or background DO. Any changes in the transport of background DO arising as a result of the plume operation will represent the effect of the oxygenation system mixing the water column in the N-basin. The layers existing between the ED and the DMPR in the N-basin will become thinner as a result of plume entrainment. They will also become shallower as a result of the plume detraining water into the ambient near the ED, where the layers become thicker and displace the shallower layers upwards. As a result of the plume-driven changes in layer thickness and depth in the N-basin, horizontal density differences will develop across the channel, leading to long-term convective exchange between the two basins.

To understand the relative effects of the plume and internal seiches as drivers of inter-basin oxygen transport, two additional scenarios were simulated using synthetic forcing (Table 2). The injected plume DO was tracked in both cases. In the first scenario (Scenario P), the wind forcing, and hence the internal seiches, was assumed to be negligible and the mass exchange was solely due to plume-induced circulation. In the second scenario (Scenario IW), the wind forcing was the same as in the reference scenario and it was assumed that operation of the bubble-plume diffuser only introduced oxygen, but did not induce circulation. In this last simulation, the water parcels were not relocated in the plume sub-model, and oxygen was simply added to the detrainment cell through a zero-order source term in the oxygen transport equation.

3 Results and Discussion

3.1 Large-scale distribution of plume-injected oxygen

Some of the DO transported between the basins during the reference simulations was due to the spatial gradients prevailing in the hypolimnion at the beginning of the study period (Fig. 1). The differences in DO concentration between the hypolimnia of the N- and S-basins increased as a result of the oxygen injected through the plume. The bubbles rise to a depth of 6-7 m (the depth of maximum plume rise DMPR), above the sill level. The plume water falls back from there to the equilibrium depth ED (varying from $z = -20$ m to $z = -12$ m in the course of the simulations), where the oxygen-enriched water is detrained to form horizontal intrusions centered at ED (Fig. 2a). The oxygenated water first replenished the deepest 25 m of the N-basin, below the

metalimnion (Fig. 2b), as a result of the plume induced basin-scale circulation. Once the oxygen reached the sill level, it moved laterally into the S-basin (Fig. 2c) as an intrusion centered at a depth of 10 m (details in the Supporting Information). A sequence of plots representing the spatial distribution of injected oxygen and the isotherm displacement at different times during a typical southerly wind event are shown in Figs. 2c-h. Note that only part of the oxygen travelling south along the channel remains in the S-basin at the end of the wind event. These plots suggest that, indeed, cross-basin oxygen transport is tightly linked to wind-driven large-scale motions.

3.2 Wind-driven internal oscillations and instantaneous inter-basin exchange flows

The initial response to the southerly wind forcing along the thalweg of the lake is illustrated in Fig. 2 and is characterized by the isotherms rising in the upwind end while falling in the downwind end of each basin. This is shown in Figs. 2d under realistic forcing and also, as an example, in Fig. 2i under a hypothetical 12-hour southerly wind event. This mode V1 response degenerates and becomes V2, shortly after the wind peaks, as the lower metalimnion rebounds faster than the upper metalimnion (Imam et al., 2013). As a result, the metalimnion widens at the upwind end of each basin (Figs. 2e under realistic forcing and 2j under the hypothetical wind event). Based on the analysis of lake (L_N) and Wedderburn (W) numbers (Monismith, 1986; Stevens & Imberger, 1996) for the N- and S-basins (Fig. 3b-c), one expects the lake response to wind forcing to be largely dominated by mode V2, with the lower metalimnetic layers remaining horizontal, hence, confining the hypolimnion to the bottom of the basin (weak mode V1, $L_N \gg 1$), and, the upper metalimnion rising near the upwind end (strong mode V2, $W < 1$). The displacements of the upper metalimnion (Δh) in the predominant mode V2 induced by southerly winds in the south end of the N-basin, calculated from estimates of W (Shintani et al., 2010), are expected to be approximately 2 m. In the S-basin, in turn, the isotherms on the northern end only compressed at those times and did not exhibit large displacements. As a result, temperature gradients are expected to develop across the central channel in a range of depths h extending from the bottom of the metalimnion ($h = 8$ m) to a depth 2 m above the top of the metalimnion ($h \sim 2$ m). The simulated horizontal temperature gradients across the channel, in fact, were particularly noticeable between 3 and 8 m from the surface (Fig. 3d), alternating in sign as a result of the strongly diurnal periodicity of the wind forcing (Fig. 3a). As a result of the baroclinic forcing resulting from the large-scale tilting of isotherms, and even without the direct

frictional effect of the wind, an oscillatory two-layer exchange flow developed in the channel, as is shown in the along-channel velocity field (Fig. 3e). Note that strong northward and southward currents alternate near the surface and the bottom, with periods close to 24h. This two-layer exchange (V1 mode) was responsible for almost 70% of the velocity variance in the channel. This contribution of the different flow modes to the velocity variance was estimated using principal component analysis applied to the observed and simulated velocity profiles at site NC (see location in Fig. 1). In this analysis, the raw signal is decomposed into a set of empirical modes (EOF empirical orthogonal functions) each one affected by time-variable amplitudes that account for the deviations around the time-averaged profile.

3.3 Drivers of residual inter-basin exchange flows

The simulated velocity profiles at site NC under the different forcing scenarios (full-, P- and IW-) were averaged in time over the study period and compared with the observed time-averaged profiles (Fig. 4a). The simulated profiles in the full- and IW-forcing scenarios were both similar to the observed profiles, with water flowing northward (away from the channel) at the surface and near the bottom, and southward (into the channel) at mid-depths. These profiles differed from the time-averaged circulation in scenario P (Fig. 4a, thin dashed line). The latter represents the plume-driven circulation with water flowing southward (into the channel) near the bottom, not northward as observed in the field. In fact, the observed velocities and the simulated plume-driven velocities had opposite directions at nearly all depths in the channel. Note also that the magnitude of the time-averaged flow rates in the IW-simulations are greater than those in the reference simulation. These differences are the result of the plume and the internal seiche dynamics forcing the water in opposite directions within the channel. These results demonstrate that internal seiche pumping, and not the plume as the empirical analysis suggests, was the dominant driver of the long-term averaged circulation observed at site NC.

3.4 Wind-driven residual inter-basin exchange flows

While wind forcing appears to be the main driver of the residual circulation as observed at site NC, it is not clear that the three-layer structure of the residual circulation could result from the two-layer exchange patterns that dominate the instantaneous velocity fields in the channel (see Fig. 3 and Supporting Information). Even more puzzling is the fact that the time-averaged

profiles at northern and southern ends of the channel did not exhibit the same pattern (Fig. 4b). The residual circulation was negligible at the center, but stronger near the ends. Also, the residual circulation at the S- (site SC) and N-ends (site NC) had opposite directions: the time-averaged velocity profile on both ends exhibit flows into the basins and away from the channel in the upper and lower parts of the water columns and into the channel at mid-depths. These changes in the time-averaged velocity profiles along the channel can be understood if one considers a simplified two-layer inviscid description of the flow field in a rectangular channel connecting two (N- and S-) basins, with the interface exhibiting out-of-phase sinusoidal oscillations on both ends as a result of wind-driven internal seiches on the N- and S-basin, and the velocity field being described as a sequence of quasi-stationary states with the two layers flowing in opposite directions (see additional details in Supporting information). The quasi-stationary assumption is reasonable as long as the adjustment time (T_a), i.e., the length of time it takes for internal perturbations occurring at either end of the channel to propagate to the other end, is short compared to the time scale of generation of such perturbations. The latter can be taken as a quarter of the first mode internal wave period, which, given the diurnal periodicity of the wind forcing, can be taken as $T_i/4 \sim 6$h (Fig. 3a). The former can be estimated from the speed of internal perturbations, c_i, calculated as $(g'h_1h_2/(h_1+h_2))^{1/2}$, where g' is the reduced acceleration of gravity, h_1 is the thickness of the upper layer and h_2 the thickness of the lower layer. For $g' = 11.5{\times}10^{-3}$ m s^{-2}, $h_1 = 5$ m and $h_2 = 5$ m (see Fig. 1), $c_i \approx 0.09$ m s^{-1}, and the adjustment time $T_a = 2.4$ h $< T_i/4$. In a quasi-stationary state, the flow rates in the upper or lower layer should not vary along the channel. The net flow in either direction will be zero at any given time, so that water is conserved on the N- and S- basins.

Figure 5 shows the evolution of the velocity profiles at the N-end, center and S-end of a 10m deep channel as calculated with the simplified description of channel flow, and, assuming maximal flow rates (per unit width) of 0.5 m^{2}s^{-1} and maximal interfacial deflections of 2 m as observed in Amisk Lake (see Figs. 2 and 3). Under southerly wind forcing, when the interface deepens near the S-end of the channel and rises near the N-end (e.g., Figs. 2i,k), water flows northward near the surface and southward below the interface. The flow in the upper layer accelerates towards the N-end as a result of the rising of the interface and the consequent narrowing of the upper layer (e.g., Fig. 5a for $tT^{-1} < 0.25$). Flow in the lower layer, in turn, accelerates towards the S- end as the lower layer narrows (e.g., Fig. 5c for $tT^{-1} < 0.25$). Note that

the maximum velocities occur near the surface at the N-end, near the bottom at the S-end, and in both cases, those maximal velocities were away from the channel (Fig. 4b, Fig. 5a,c). Under calm conditions, the flow patterns are reversed, the maximum velocities are expected near the bottom in the N-end, and near the surface in the S-end, and again, the directions of the flows will be directed away from the channel (e.g., Figs. 5a,c for $0.25 < tT^{-1} < 0.75$). These flow patterns under windy and calm conditions are consistent with the simulations conducted with the 3D model (Fig. 2k-l). The average velocity profiles during any given cycle at the two ends of the channel have a three-layer structure (Figs. 5d and 5f). The time-averaged profile in either the S- or the N- ends of the channel exhibited flows into the basins and away from the channel in the upper and lower parts of the water columns, and towards the channel at mid depths as in Fig. 4b. Note that the residual flow pattern in the N-end is consistent with the observations (Fig. 4a). The vertical structure of the time-averaged velocity profile, the magnitude of the averaged velocities and the extension of the layers, will change depending on (1) the phase lag Φ between the velocity and interfacial displacements (Figs. 5d-f) and (2) the amplitude A of those displacements (Figs. 5g-i). Those parameters (phase and amplitude) will likely vary depending on the lake geometry, forcing and the site of the observations. Note that, it is only for $\Phi = \pi/2$ or $A \approx 0$ that the averaged velocity profile does not exhibit any vertical structure.

3.5 Decomposition of inter-basin oxygen transport

In their empirical analysis, Lawrence et al. (1997) argued that oxygen during the one-month study period (June 1991) was transported from the N- to the S-basin as a result of two mechanisms: (a) the plume-induced large-scale circulation and (b) the effect of internal seiches pumping water across the sill. The "persistent and long-term circulation" observed at site NC below the thermocline (Fig. 4a) was attributed to the plume inducing circulation, based on the results of earlier plume models predicting a unique intrusion, which was assumed to develop above the sill depth, near the top of the metalimnion. Oxygen loading rates associated with the long-term circulation were calculated from observed residual velocities, channel widths and DO concentrations at each depth in the channel. The latter were estimated from the averaged DO concentration profiles collected in the N basin during the one-month study period, in which the concentration increased 3.6 g m^{-3} from a depth of 12 m to 5 m. According to those calculations,

the long-term channel circulation would transport an average of $\approx$ 200 kg d^{-1} of oxygen from the N- to the S- basin below the thermocline during the month of July 1991 (see Lawrence et al., 1997). To assess the oxygen exchanged as a result of the internal seiche pumping, it was assumed that the volume of water flowing southward through section NC between any two flow reversals (event) would only inject oxygen into the S-basin if its excursion length (distance travelled by a water parcel during that period based on the ADCP records) exceeded the length of the channel (see Eq. 4 in Lawrence et al. (1997)). To estimate the oxygen exchanged, the volume of water effectively reaching the S-basin during any given event was multiplied by the average difference in DO concentration observed in the upper hypolimnion of the two basins (~1 g m^{-3}). The estimated oxygen load was 60 kg d^{-1}.

The "empirical analysis", as described above, is based on decomposing the time series of flow (Q) and oxygen (O) concentrations into a long-term or time-averaged component (denoted by an overbar) plus a short-term or fluctuating component (identified by a prime symbol). For Q, this decomposition is as follows:

$$Q_k(n) = \overline{Q}_k(n) + Q'_k(n) = \frac{1}{N}\sum_{i=1}^{N} Q_k(i) + \left(Q_k(n) - \frac{1}{N}\sum_{i=1}^{N} Q_k(i) \right) \tag{2}$$

Here k is the bin or depth interval in a profile, n is the time interval when the profile is taken, and N is the number of time intervals within the period analyzed. The oxygen profiles at site NC can be similarly decomposed as

$$O_k(n) = \overline{O}_k + O'_k(n) \tag{3}$$

The averaged transport rate (or loading) during the study period below any given depth z (from layer k_z, at z, to k_m, at the bottom), L_z, could then be expressed as:

$$L_z = \frac{1}{N}\sum_{k=k_z}^{k_m}\sum_{n=1}^{N} O_k(n) \cdot Q_k(n) = \sum_{k=k_z}^{k_m} \overline{O}_k \cdot \overline{Q}_k + \frac{1}{N}\sum_{k=k_z}^{k_m}\sum_{n=1}^{N} O'_k(n) \cdot Q'_k(n) \tag{4}$$

The first component on the right-hand side represents the transport associated with the "persistent, long-term average" flows (Lawrence et al., 1997). It will be referred to as the long-term or time-averaged component of transport. The second (or fluctuating) component accounts for the fact that depending on whether the flow is northward (positive) or southward (negative), the observed oxygen concentration may change as a result of differing hypolimnetic oxygen levels between the N- and S-basin. Hence, this second term represents the contribution of internal-seiche pumping.

In Fig. 6, the long-term and fluctuating transport profiles are shown for different scenarios (Table 2), as calculated from simulated results at site NC. The time-averaged oxygen profiles below 5 m (O_{5-12}) are also shown. Table 2 provides the average loading rates below 5m, which was taken as the depth of the thermocline, as in Lawrence et al. (1997). The time-averaged full loading rate of oxygen below 5 m in the reference simulation was -260 kg d^{-1} (Table 1). This estimate is within 20% of the results of the empirical analysis. The fluctuating component was of similar magnitude (-200 kg d^{-1}) and also southward. Most of the fluctuating transport is associated with the injected-oxygen (-191 kg d^{-1}). The magnitude of the time-averaged transport of injected oxygen was ≈ 5 times less than the fluctuating component, but northward (Table 2). This is in the same direction of the time-averaged flows near the bottom, where the averaged concentration of injected DO was greater (Figs. 6b). Of the total load of oxygen transported through section NC below 5 m, ca. 30% was injected oxygen, the remaining being background oxygen.

The net-transport rate of injected plume-DO in the IW- and P- scenarios was -30 kg d^{-1}, approximately 20% of the net transport rate in the reference simulation, and, also southwards. Note, though, that the southward net transport was largely attributed to the fluctuating component in scenario IW, while the average load associated with the long-term circulation was, in this case, northward (Table 2 and Fig. 6c). By contrast, in scenario P, the net southward transport rate was largely determined by the time-averaged component (Table 2 and Fig. 6d). The different sign of the long-term oxygen transport in scenario P compared to that in the reference simulation arises as a result of the plume forcing the oxygenated water to flow southward near the bottom and the non-oxygenated water above to flow northward (see Fig. 4a). As a result of the plume-induced circulation being opposite to that of internal seiching (see Fig. 4), less shear is predicted in the averaged flow profile in the reference simulation compared to the IW scenario, with weaker northward flows near the bottom and also weaker southward flows

above. In consequence, a 30-40% reduction of the time-averaged southward transport (from -420 to -300 kgO d^{-1}) of background oxygen below 5 m occurs as a result of the plume dynamics (Table 2).

The previous calculations, based on numerical simulations, are consistent with those in the 'empirical' analysis in that the estimates of the time-averaged loadings below 5m are similar. This agreement arises as a result of both (1) the agreement between modeled and time-averaged velocity profiles (Fig. 4) and (2) the time-averaged vertical DO gradients between 12 and 5 m being comparable to those used in the empirical analysis (see Fig. 6a). The analysis presented here, though, differs from the earlier interpretation in several aspects. First, the time-averaged flow profile is largely attributable to internal seiching, and not to plume dynamics. Plume induced mixing will lead to a steady southward motion near the bottom, instead, carrying injected oxygen at a rate of ca. -33 kg d^{-1} (see results for P-scenario in Table 2). This is almost 20% of the total load of injected oxygen calculated in the reference simulations. However, the magnitude of this southward steady plume-driven motion is low compared to the instantaneous and time-averaged wind-driven motions, and, will therefore be difficult to observed. The second difference lies in the estimated magnitude of the internal-seiche driven transport (the fluctuating component) which is 2-3 times larger than the 'empirical' estimates. The arguments, based on estimates of the excursion lengths, to calculate inter-basin oxygen transport were intended to remove the buffering effect of the channel between the N- and S- basins, given the fact that velocities were not observed on the southern end of the channel. In Table 2, we have included estimates of injected-oxygen transport calculated from the reference simulations at a cross section in the southern end of the channel (site SC in Fig. 1). Note that the injected-plume loadings at site SC are consistent with those calculated at NC (ca. -150 kg d^{-1}). The fluctuating component is also southward, as at NC, but its magnitude is reduced to almost 50% of the calculated value at NC. The sign of the time-averaged component, in turn, changes to northward at SC. This is consistent with the form of the averaged velocity profile shown in Fig. 4.

3.6 Role of plume and internal wave forcing in the inter-basin transport

The plume-DO concentration from 5 to 12 m at NC (O_{5-12}) and the mass of plume-DO in the S-basin (ΔO) are shown as a function of time in Fig. 7 for the three forcing scenarios considered. In

all cases, during the first 4-5 days of the simulation, the concentration above the sill and the average loading into the S-basin remained negligible (Fig. 7a). This is the period of time that the oxygenated plume water takes to fill the volume in the N-basin between the estimated ED ($z \approx$ -21 m at the onset of the simulations) and the sill level (z = -12 m), at the detrainment rate predicted by the plume model (ca. 11 $m^3\,s^{-1}$). The simulated O_{5-12} increased in the reference scenario rapidly after day 186 to ca 0.8 g m^{-3} on day 200. It increased thereafter, but at half the initial rate so that at the end of the simulation period O_{5-12} was 1.2 g m^{-3}. These changes represent the plume-induced vertical transport of oxygen from the equilibrium depth, where it is injected, upwards to the DMPR. Most of the injected plume-DO in scenario IW remained confined below the metalimnion in the N- basin (Figs. 7a and 8c). The vertical transport of oxygen from the ED to the sill in this scenario occurred largely by turbulent diffusion. The effective vertical diffusivity K_{eff} in the hypolimnion, estimated as in McGinnis et al. (2004) from the sequence of area averaged temperature profiles in the N-basin, was $O(10^{-3})$ m^2s^{-1}. By contrast, the estimates of K_{eff}, calculated from the simulations in the full forcing scenario, were two orders of magnitude larger, representing the net effect of the plume-driven relocation of water parcels in the water column. The total mass of oxygen exchanged during the 30-day simulated period in Scenario IW (ΔO_{IW}) was only 20-25% of that calculated for the reference scenario, ΔO_0 (Fig. 7b). In Scenario IW, horizontal exchange occurred only during the strongest wind events (i.e., day 200 or 207, Fig. 7b) when the oxygenated layers upwelled to the sill level. In Scenario P, the plume DO could effectively reach the sill level (see Fig. 7b and 8b), but the total mass of oxygen transported ΔO_P was only 30-40% of ΔO_0 (Fig. 7a). The estimates of K_{eff} were similar to that calculated for the reference scenario, which suggests that the limiting process preventing oxygen from moving it southward was horizontal transport. In Scenario P, internal wave pumping was nonexistent, and oxygen was only transported horizontally to the S-basin through turbulent diffusion along the channel. These results suggest that the internal wave motions themselves cannot explain the transport of oxygen between the basins. Inter-basin transport depends on the plume dynamics to move the oxygen vertically from the ED where it is injected to near-sill levels, where internal wave pumping is the major driver of horizontal transport (Figs. 7b and 8).

The time series of O_{5-12} in the reference simulation exhibits oscillations around its averaged value that represent the effect of internal seiches raising and lowering oxygenated water. The

amplitude of the oscillations increases with the averaged value, being even, of the same order of magnitude at times. Note, for example, the oscillations in O_{5-12}, with amplitudes of $O(1)$ gO m^{-3}, simulated on days 206-207 in response to the strong wind events occurring at that time. During that period of 2 days, almost 800 kg of plume-DO were transported to the S-basin ($\approx$ 400 kg d^{-1}) through seiche-pumping. This can be considered a reasonable and realistic estimate given that the O_{5-12} at that time was ca. 1 g m^{-3} (Fig. 7a), which is the average difference in DO concentration between the N- and S-basin, as reported in Lawrence et al. (1997). To make comparable and realistic estimates of oxygen loads during any given period of time in July, with averaged concentrations O_{5-12} in the range from 0.8 and 1 g m^{-3}, a series of 30-day simulations were conducted with different starting dates. In those simulations, the solar radiation (missing prior to day 190 in 1991) was reconstructed from the observed daily temperature ranges (as in Hargreaves & Samani, 1982;1985), and, assuming hourly variations similar to the theoretical astronomical calculations. Different starting days were tested, from 165 to 190 with a 5-day interval. The 5-day interval corresponds to the filling period (see above). Oxygen loads were estimated in those simulations from the cumulative transport through the cross-section NC from day 20 to 25 after the beginning of the simulation, when the concentrations were ca. 1 g m^{-3}. The results are shown in Table 3. The loading estimates varied from 107 kg d^{-1} (between days 210 and 215) to almost 452 kg d^{-1} (between days 185 to 190), with an average rate of 240 kg d^{-1}. A total of 7t of oxygen could have been injected in the S-basin during the 30-day period from day 185 to 215, as calculated from the results of Table 3. The maximal rates coincide with those periods with the strongest wind events, and, hence, with large amplitude internal seiches (around days 187, 192 and 206). Nearly 30% of the 7t, for example, was exchanged during the strongest event, between days 186 to 188, when the estimated loading rate was ca. 1000 kg d^{-1}. These results agree, in general, with Lawrence et al. (1997) who noted that internal seiche-driven transport would be episodic and concentrated during periods of strong wind.

3.7. Inter-basin transport during the ice-free period and effect of thermocline depth

Assuming that the average load of ca. -240 kg d^{-1} estimated above for July applies also during the ice-free period, from May to September, the mass of injected oxygen ending in the S-basin through internal seiche-pumping would be approximately 36t. This is nearly 40% of the mass of

oxygen that was estimated earlier to move from the N to the S basin during one year as a result of operating the oxygenation system (see Lawrence et al., 1997). The effects of the sediment oxygen demand (SOD) on these calculations are probably minor. To avoid this effect, we have restricted our calculations to times when the average concentration of injected oxygen at NC was ca. 1 g m^{-3}. This is the observed averaged concentration difference between the hypolimnion of the N- and S- basins, which can be attributed to the plume. To further support our hypothesis regarding the negligible effect of SOD, we repeated the 30-day reference simulations with SOD included in the bottom cells as a zero-order sink term of constant magnitude = 0.8 g m^{-2}d^{-1} (as reported by Prepas et al., 1997). The inter-basin exchange of injected-oxygen at section SC in those simulations and the same estimates in the reference simulation differ by less than 4%. Our calculations, though realistic for the conditions prevailing in July, could be underestimating internal-seiche driven oxygen loads into the S-basin during other months when observations were not available. Our calculations are based on the assumption that stratification and wind forcing (the magnitude and duration of the wind events) remain stable from May to September. The first assumption is obviously wrong (see Webb et al. 1997, for example). The results shown in Table 3 indicate that transport rates will change depending on the amplitude of the internal seiches, with larger rates occurring in response to stronger wind events. If we consider that both basins oscillate independently, and, assuming a two-layer model for stratification, the expected maximum displacement of the thermocline, Δh, across the channel can be estimated as (e.g., Shintani et al., 2010)

$$\Delta h \approx \frac{h}{W} = \frac{\rho_0 u_*^2 L}{g \Delta \rho_{12} h} \tag{5}$$

as a function of the thickness of the upper layer h, the fetch L and density contrast between the upper and lower layer $\Delta \rho_{12}$. Here, g is the acceleration of gravity and ρ_0 is a reference density. The displacement is proportional to both the squared friction velocity u_* and the inverse of the thermocline depth. The magnitude of the baroclinic forcing across the channel, driving the exchange flows, in turn, will scale as

$$F_b = -\frac{g}{\rho_0} \int_z^\zeta \frac{\partial \rho}{\partial x} dz' \approx \frac{g\Delta\rho_{12}}{\rho_0} \frac{\Delta h}{L_c} H_c \tag{6}$$

where L_c and H_c are the length and depth of the channel. If we substitute Eq. 5 in 6, and assume that oxygen transport is proportional to the magnitude of the exchange flows, the loading of oxygen should scale as

$$\Delta O \approx \frac{u_*^2 L}{h} \frac{H_c}{L_c} \tag{7}$$

Note that oxygen transport depends on the geometry of the basins and that of the connecting channel, as well as the stratification and the strength of the wind forcing. The length scales in Eq. 7 are fixed in Amisk Lake, but both h (depth of the upper layer) and the friction velocity u_* (depending on the wind) will vary depending on the month. In spring, for example, the depth of the thermocline h tends to be shallower (e.g., Webb et al., 1997). The winds are also expected to vary. Given the lack of local wind records in Amisk Lake, we studied a 10-year wind data set from Atmore AGDM meteorological station (54.7802°N, -112.8248) located $\approx$ 24 km northwest from the lake, which is publicly accessible. The data set was analyzed to isolate individual events when wind speeds were larger than the 75-percentile of the records (3.7 m s^{-1}) for at least 6 h (approx. a quarter of the internal wave period in summer in Amisk Lake). The number of events, their duration and average magnitude are shown in Table 4. Even though those estimates are not for Amisk Lake, and will likely vary from site to site, they suggest that wind forcing does indeed exhibit seasonal changes in the area of interest. Note that the number of strong events were ca. 50% more frequent in May compared to July (15 events per month in May vs. 10 in July), being their average speed of similar magnitude (approximately 5 m s^{-1}). Given these changes in wind forcing, internal-seiche driven transport could be larger in spring in comparison to mid-summer conditions. Moreover, given the weak stability of the water column in May, it seems plausible that stratification could break during some of those strong events. The plume might be injecting oxygen directly into the epilimnion during those events, where, as a result of advection and shear dispersion, the transport of plume-DO could be faster (see Priet-Mahéo et al., 2019). Hence, either as a result of more frequent strong wind events, or, as a result of the increased horizontal

transport in the epilimnion when the plume-DO reaches the near-surface layers, the loading rates into the S-basin could be larger in spring than estimated for the month of July. This is in agreement with earlier results (see Prepas & Burke, 1997) that suggest that the loading of oxygen in spring was larger than later in the summer.

Lawrence et al (1997) argued that DO inter-basin exchange due to IW transport and plume circulation in Amisk Lake was possible given that the thermocline depth is shallower than the depth of the sill connecting both basins. This is consistent with field and modeling studies evaluating inter-basin exchanges in other systems. For example, Umlauf & Lemmin (2005) showed through field and numerical experiments that the inter-basin-exchanges due to Kelvin waves between the main basin and the shallower Petit Lac in Lake Geneva (46.5 ºN) are responsible for maintaining high oxygen levels in the hypolimnion of the Petit Lac when both basins are stratified, and thus for this lake, when the thermocline is shallower than the depth of the shallower basin. When the metalimnion is shallower than the depth of the sill of Mainau, connecting Lake Überlingen and the main basin of Upper Lake Constance (47.5 ºN), Appt et al. (2004) showed through their numerical simulations, that Kelvin-type waves after wind events also lead to stronger exchanges between the two basins. And Laval et al. (2008) also suggested that the observed wind events during the stratification period in Quesnel Lake (52º N) lead to a two-way advective transport over the sill separating the western and main basins of the lake and each event was responsible for up to 30% of hypolimnetic water renewal of the western basin. However, the condition of a thermocline that is shallower than the sill connecting treated and non-treated basins as in Amisk Lake is not necessarily met in other systems. The position of the thermocline with respect to the sill is a known limiting factor for the exchange of hypolimnetic water between different basins in two-basin and multi-basin lakes (e.g., Laval et al., 2008; Robertson & Ragotzkie, 1990). Once the thermocline descends past the sill level, the exchange of hypolimnetic water is commonly restricted to wind events that are capable of upwelling the thermocline past the sill level (e.g., Robertson & Ragotzkie, 1990; van Senden & Imboden, 1989). Overall, these results indicate that higher hypolimnetic DO transfers are expected in two- or multi-basin lakes with long fetches (larger isotherm displacement for a given wind forcing), interconnected hypolimnia (thermoclines that are shallower than sill depths), and short-length and deep interconnecting channels.

4 Summary and Conclusions

A data set was collected in a two-basin lake (Amisk Lake, Canada) by Lawrence et al. (1997) in 1991, under stratified conditions, when a bubble plume was injecting oxygen in the north basin. The data were analyzed earlier (Lawrence et al., 1997) using scaling arguments and simplified models of the relevant transport processes (empirical analysis). Several reasonable assumptions were made in order to fill data gaps. In the empirical analysis, the transport of oxygen from the N-basin (where the diffuser was installed) into the S-basin could be largely explained by an existing bubble-plume induced circulation. The internal seiche pumping was of minor importance, even in summer time when internal seiching was supposed to be strongest in comparison with other seasons. Here, the results of a validated coupled bubble-plume 3D hydrodynamic and transport model of Amisk Lake are used to fill-in missing information in the field-data set, and to re-assess the relative contribution of bubble-plume induced circulation and internal seiche pumping to the inter-basin exchange of oxygen in summer. The importance of internal-seiche pumping as a driver of inter-basin exchange during the year is analyzed. The conclusions of this work are as follows:

[1] Under the conditions prevailing during the study period, the model (as configured) predicted bubble-plume injection of oxygen into the hypolimnion at a depth that varied from $z = -21$ m, at the onset of the simulations, to $z = -12$ m, was always below the sill depth. The DMPR varied from $z = -5$ m to -7 m in the simulations. Hence, the earlier interpretation of the large-scale circulation in which the southward flow between 2-9 m depth was assumed to be driven by the plume detraining water at that depth, is not supported by the simulations.

[2] The observed residual circulation in the N-end of the channel (northward in the top and bottom of the water column, and southward at mid-depth) was opposite in direction to that driven by the plume dynamics (southward in the bottom of the water column, and northward at mid-depth). Thus, the observed "persistent, long-term average circulation" cannot be attributed to the plume dynamics, in contrast to previously reported.

[3] Instantaneous velocity profiles in the channel are the result of the wind-driven internal seiches on the N- and S-basins. Strong and episodic southerly wind events aligned with the thalweg, exciting basin-scale internal seiches with isotherm displacements of 4 m and 2 m, on the S- and N- ends of the channel, respectively. As a result, oscillating baroclinic pressure

gradients developed, leading to a time-varying oscillatory two-layer exchange flow in the channel.

[4] The three-layer residual circulation observed by Lawrence et al. (1997) at the N-end of the channel (northward in the top and bottom of the water column, and southward at mid-depth), and the changes in the residual circulation predicted by the 3D model along the channel are interpreted as a result of time-variable exchange flows, driven by out-of-phase oscillations of the thermocline occurring on both ends of the channel driven by internal seiches. A simple two-layer description of the channel flow is used in this analysis.

[5] The inter-basin transport of oxygen was estimated from simulated velocity and dissolved oxygen concentrations at cross section NC. The transport was decomposed into (1) a time-averaged component, representing the "persistent, long-term average flows" in the earlier results of Lawrence et al. (1997), and, (2) a fluctuating component, representing the effect of internal seiche-pumping. The magnitude of the time-averaged component below the thermocline as calculated from the simulations, was comparable to the estimates in the "empirical analysis" and also southwards. Our interpretation of the time-averaged exchange differs from that arising in the empirical analysis in that here it is attributed to internal seiche-pumping and not to plume-induced circulation. The fluctuating component is of similar magnitude, being largely the result of the internal-waves carrying injected-oxygen southwards. Almost 65% of the oxygen transported from the N- to the S-basin below the thermocline is background oxygen and not injected-oxygen, as assumed in the empirical analysis.

[6] While the horizontal exchange of oxygen is largely driven by internal seiche-pumping, the vertical transport of the injected oxygen, from the entrainment depth to the layers above the sill, is primarily controlled by large-scale, plume-induced circulation. Both mechanisms, in interaction, are key to understanding the inter-basin exchange of oxygen. Without the vertical transport of oxygen by the plume-induced circulation, the mass of oxygen transported to the south basin only reached 40% of the total oxygen transported in the reference simulation.

[7] Nearly 40% of the oxygen transported from the N- to the S-basin during one year could be attributed to internal-seiche pumping during the ice-free period under stratified conditions. The magnitude and importance of internal-seiche pumping on inter-basin transport will vary depending on the wind forcing (frequency, duration and intensity of wind events), the position of the thermocline and the physical dimensions of the connecting channel. According to our

estimates, the largest loadings in Amisk Lake will likely occur during spring time, which agrees with earlier results (Lawrence et al., 1997; Prepas & Burke, 1997).

Acknowledgements

References

Appt, J., Imberger, J., & Kobus, H. (2004). Basin-Scale Motion in Stratified Upper Lake Constance. *Limnology and Oceanography*, *49*(4), 919–933. https://doi.org/10.4319/lo.2004.49.4.0919

Asaeda, T., & Imberger, J. (1993). Structure of bubble plumes in linearly stratified environments. *Journal of Fluid Mechanics*, *249*, 35–57. https://doi.org/10.1017/S0022112093001065

Bombardelli, F. A., Buscaglia, G. C., Rehmann, C. R., Rincón, L. E., & García, M. H. (2007). Modeling and scaling of aeration bubble plumes: A two-phase flow analysis. *Journal of Hydraulic Research*, *45*(5), 617–630. https://doi.org/10.1080/00221686.2007.9521798

Bryant, L. D., Gantzer, P. A., & Little, J. C. (2011). Increased sediment oxygen uptake caused by oxygenation-induced hypolimnetic mixing. *Water Research*, *45*(12), 3692–3703. https://doi.org/10.1016/j.watres.2011.04.018

Hargreaves, G. H., & Samani, Z. A. (1982). Estimating Potential Evapotranspiration. *Journal of the Irrigation and Drainage Division*, *108*(3), 225–230. https://doi.org/10.1061/JRCEA4.0001390

Hargreaves, G. H., & Samani, Z. A. (1985). Reference Crop Evapotranspiration from Temperature. *Applied Engineering in Agriculture*, *1*(2), 96–99. https://doi.org/10.13031/2013.26773

Hodges, B. R., Imberger, J., Saggio, A., & Winters, K. B. (2000). Modeling basin-scale internal waves in a stratified lake. *Limnology and Oceanography*, *45*(7), 1603–1620. https://doi.org/10.4319/lo.2000.45.7.1603

Imam, Y. E., Laval, B. E., & Lawrence, G. A. (2013). The baroclinic response to wind in a small two-basin lake. *Aquatic Sciences*, *75*(2), 213–233. https://doi.org/10.1007/s00027-012-0268-1

Laval, B. E., Morrison, J., Potts, D. J., Carmack, E. C., Vagle, S., James, C., et al. (2008). Wind-driven Summertime Upwelling in a Fjord-type Lake and its Impact on Downstream River Conditions: Quesnel Lake and River, British Columbia, Canada. *Journal of Great Lakes Research*, *34*(1), 189–203. https://doi.org/10.3394/0380-1330(2008)34[189:WSUIAF]2.0.CO;2

Lawrence, G. A., Burke, J. M., Murphy, T. P., & Prepas, E. E. (1997). Exchange of water and oxygen between the two basins of Amisk Lake. *Canadian Journal of Fisheries and Aquatic Sciences*, *54*(9), 2121–2132. https://doi.org/10.1139/f97-235

Lee, J. H. W., & Chu, V. (2012). *Turbulent jets and plumes. A Lagrangian approach*. New York, USA: Springer Science & Business Media.

Little, J. C., & McGinnis, D. F. (2001). Hypolimnetic oxygenation: Predicting performance using a discrete-bubble model. In *Water Science and Technology: Water Supply* (Vol. 1, pp. 185–191). IWA Publishing. https://doi.org/10.2166/ws.2001.0083

McGinnis, D. F., Lorke, A., Wüest, A., Stöckli, A., & Little, J. C. (2004). Interaction between a bubble plume and the near field in a stratified lake. *Water Resources Research*, *40*(10). https://doi.org/10.1029/2004WR003038

Mitchell, P., & Prepas, E. E. (1990). Amisk Lake. In P. Mitchell & E. E. Prepas (Eds.), *Atlas of Alberta Lakes* (pp. 225–231). Edmonton: The University of Alberta Press.

Monismith, S. (1986). An experimental study of the upwelling response of stratified reservoirs to surface shear stress. *Journal of Fluid Mechanics*, *171*(1), 407. https://doi.org/10.1017/S0022112086001507

Prepas, E. E., & Burke, J. M. (1997). Effects of hypolimnetic oxygenation on water quality in Amisk Lake, Alberta, a deep, eutrophic lake with high internal phosphorus loading rates. *Canadian Journal of Fisheries and Aquatic Sciences*, *54*(9), 2111–2120. https://doi.org/10.1139/f97-125

Prepas, E. E., Field, K. M., Murphy, T. P., Johnson, W. L., Burke, J. M., & Tonn, W. M. (1997). Introduction to the Amisk Lake Project: oxygenation of a deep, eutrophic lake. *Canadian Journal of Fisheries and Aquatic Sciences*, *54*(9), 2105–2110. https://doi.org/10.1139/f97-119

Priet-Mahéo, M. C., Ramón, C. L., Rueda, F. J., & Andradóttir, H. Ó. (2019). Mixing and internal dynamics of a medium-size and deep lake near the Arctic Circle. *Limnology and Oceanography*, *64*(1), 61–80. https://doi.org/10.1002/lno.11019

Robertson, D. M., & Ragotzkie, R. A. (1990). Thermal Structure of a Multibasin Lake: Influence of Morphometry, Interbasin Exchange, and Groundwater. *Canadian Journal of Fisheries and Aquatic Sciences*, *47*(6), 1206–1212. https://doi.org/10.1139/f90-140

Schladow, S. G. (1992). Bubble plume dynamics in a stratified medium and the implications for water quality amelioration in lakes. *Water Resources Research*, *28*(2), 313–321. https://doi.org/10.1029/91WR02499

Schladow, S. G., & Fisher, I. H. (1995). The physical response of temperate lakes to artificial destratification. *Limnology and Oceanography*, *40*(2), 359–373. https://doi.org/10.4319/lo.1995.40.2.0359

Van Senden, D. C., & Imboden, D. M. (1989). Internal seiche pumping between sill-separated basins. *Geophysical & Astrophysical Fluid Dynamics*, *48*(1–3), 135–150. https://doi.org/10.1080/03091928908219530

Shintani, T., de la Fuente, A., de la Fuente, A., Niño, Y., & Imberger, J. (2010). Generalizations of the Wedderburn Number: Parameterizing Upwelling in Stratified Lakes. *Limnology and Oceanography*, *55*(3), 1377–1389. https://doi.org/10.4319/lo.2010.55.3.1377

Singleton, V. L., & Little, J. C. (2006). Designing hypolimnetic aeration and oxygenation systems - A review. *Environmental Science and Technology*. American Chemical Society. https://doi.org/10.1021/es060069s

Singleton, V. L., Gantzer, P., & Little, J. C. (2007). Linear bubble plume model for hypolimnetic oxygenation: Full-scale validation and sensitivity analysis. *Water Resources Research*, *43*(2). https://doi.org/10.1029/2005WR004836

Singleton, V. L., Rueda, F. J., & Little, J. C. (2010). A coupled bubble plume-reservoir model for hypolimnetic oxygenation. *Water Resources Research*, *46*(12). https://doi.org/10.1029/2009WR009012

Smith, P. (2006). *A Semi-Implicit, Three-Dimensional Model of Estuarine Circulation*. Open File Report 2006-1004, USGS, Sacramento, USA.

Socolofsky, S. A., Bhaumik, T., & Seol, D.-G. (2008). Double-Plume Integral Models for Near-Field Mixing in Multiphase Plumes. *Journal of Hydraulic Engineering*, *134*(6), 772–783. https://doi.org/10.1061/(ASCE)0733-9429(2008)134:6(772)

Stevens, C., & Imberger, J. (1996). The initial response of a stratified lake to a surface shear stress. *Journal of Fluid Mechanics*, *312*, 39–66. https://doi.org/10.1017/S0022112096001917

Strub, P. T., & Powell, T. M. (1986). Wind-driven surface transport in stratified closed basins: Direct versus residual circulations. *Journal of Geophysical Research*, *91*(C7), 8497. https://doi.org/10.1029/JC091iC07p08497

Umlauf, L., & Lemmin, U. (2005). Interbasin exchange and mixing in the hypolimnion of a large lake: The role of long internal waves. *Limnology and Oceanography*, *50*(5), 1601–1611. https://doi.org/10.4319/lo.2005.50.5.1601

Wang, B., Lai, C. C. K., & Socolofsky, S. A. (2019). Mean velocity, spreading and entrainment characteristics of weak bubble plumes in unstratified and stationary water. *Journal of Fluid Mechanics*, *874*, 102–130. https://doi.org/10.1017/jfm.2019.461

Webb, D. J., Robarts, R. D., & Prepas, E. E. (1997). Influence of extended water column mixing during the first 2 years of hypolimnetic oxygenation on the phytoplankton community of Amisk lake, Alberta. *Canadian Journal of Fisheries and Aquatic Sciences*, *54*(9), 2133–2145. https://doi.org/10.1139/f97-120

Wüest, A., Brooks, N. H., & Imboden, D. M. (1992). Bubble plume modeling for lake restoration. *Water Resources Research*, *28*(12), 3235–3250. https://doi.org/10.1029/92WR01681

References From the Supporting Information

Amorocho, J., & DeVries, J. J. (1980). A new evaluation of the wind stress coefficient over water surfaces. *Journal of Geophysical Research*, *85*(C1), 433. https://doi.org/10.1029/JC085iC01p00433

Fischer, H. B., List, E. J., Koh, R. C. Y., Imberger, J., & Brooks, N. H. (1979). *Mixing in Inland and Coastal Waters*. New York: Academic Press.

Imam, Y. E., Laval, B. E., & Lawrence, G. A. (2013). The baroclinic response to wind in a small two-basin lake. *Aquatic Sciences*, *75*(2), 213–233. https://doi.org/10.1007/s00027-012-0268-1

Kantha, L. H., & Clayson, C. A. (1994). An improved mixed layer model for geophysical applications. *Journal of Geophysical Research: Oceans*, *99*(C12), 25235–25266. https://doi.org/10.1029/94JC02257

Mitchell, P., & Prepas, E. E. (1990). Amisk Lake. In P. Mitchell & E. E. Prepas (Eds.), *Atlas of Alberta Lakes* (pp. 225–231). Edmonton: The University of Alberta Press.

Priet-Mahéo, M. C., Ramón, C. L., Rueda, F. J., & Andradóttir, H. Ó. (2019). Mixing and internal dynamics of a medium-size and deep lake near the Arctic Circle. *Limnology and Oceanography*, *64*(1), 61–80. https://doi.org/10.1002/lno.11019

Rueda, F. J., & Schladow, S. G. (2002). Quantitative Comparison of Models for Barotropic Response of Homogeneous Basins. *Journal of Hydraulic Engineering*, *128*(2), 201–213. https://doi.org/10.1061/(asce)0733-9429(2002)128:2(201)

Wüest, A., Brooks, N. H., & Imboden, D. M. (1992). Bubble plume modeling for lake restoration. *Water Resources Research*, *28*(12), 3235–3250. https://doi.org/10.1029/92WR01681

Table 1. List of model parameter values used in the simulations (and references that justify the values used in the actual model configuration)

	Parameter	Value	Reference
λb_0 (m)	Diffuser half width	3.38	https://wldb.ilec.or.jp/Display/html/3445
r_0 (μm)	Initial bubble diameter	1500	[20-1500] μm Prepas et al. (1997)
q_0 (m^{3}s^{-1}, std. cond.)	Initial flow	$2.8 \cdot 10^{-3}$	Lawrence et al. (1997)
α_i	Entrainment coefficient inner plume	0.055	Socolofsky et al. (2008)
α_o	Entrainment coefficient outer plume	0.11	Socolofsky et al. (2008)
α_a	Entrainment coefficient from ambient	0.11	Socolofsky et al. (2008)
λ	Fraction of plume occupied by bubble	1	Milgram (1983)
F	Initial Froude number inner plume	1.6	Socolofsky et al. (2008)
F$_o$	Initial Froude number outer plume	0.1	Socolofsky et al. (2008)
γ	Momentum amplification factor	1.1	Socolofsky et al. (2008)
Δx	Cell size (m) in EW direction	50	
Δy	Cell size (m) in NS direction	50	
Δz	Cell size (m) in vertical	0.5	
Δt	Time step (s)	30	
K_h	Horizontal eddy diffusivity/viscosity (m s^{-2})	$5 \cdot 10^{-1}$	Priet-Mahéo et al. (2019)
C_d	Bottom drag coefficient	$5 \cdot 10^{-2}$	Smith (2006)

Table 2. Simulations conducted with the coupled model (Full-forcing, Scenario IW and Scenario P) and DO transport (kg/day) along the channel (positive to the N-basin and negative to the S-basin) below 5 m depth, for different tracer experiments.

Forcing scenarios	Diffuser Forcing	Wind Forcing	Traced oxygen	Initial DO concentration S-basin	Initial DO concentration N-basin	Plume oxygen load	$\sum_{k=k_z}^{k_m}\overline{O}_k \cdot \overline{Q}_k$ (1)	$\frac{1}{N}\sum_{k=k_z}^{k_m}\sum_{n=1}^{N} O'_k(n)Q'_k(n)$ (2)	$\frac{1}{N}\sum_{k=k_z}^{k_m}\sum_{n=1}^{N} O_k(n)Q_k(n)$ (3)
Full-forcing (IW + P)[a]	✓	✓	Full DO	OBS$_S$	OBS$_N$	✓	-258	-200	-458
			Background DO	OBS$_S$	OBS$_N$		-299	-11	-310
			Injected plume-DO	Zero	Zero	✓	40	-191	-151
			Injected plume-DO[(1)]	Zero	Zero	✓	-48	-106	-155
IW-forcing		✓	Full DO	OBS$_S$	OBS$_N$	✓	-369	-88	-457
			Background DO	OBS$_S$	OBS$_N$		-379	-45	-424
			Injected plume-DO	Zero	Zero	✓	11	-42	-31
P-forcing	✓		Injected plume-DO	Zero	Zero	✓	-33	-2	-35

Note. OBS$_N$ and OBS$_S$ are the dissolved oxygen profiles collected by Lawrence et al. (1997) at sites N2 and S2 (Fig. 1). The simulation with full forcing and dissolved oxygen (DO) concentration initialized as in the observations (fullDO) is the reference simulation. The DO transport (column 3) is decomposed into a time-averaged component (column 1), that represents the transport associated with the "persistent, long-term average" flows, and a fluctuating component

(column 2), that shows the contribution of internal wave pumping for the differences forcing scenarios.[a] Reference simulation. (1) Results calculated from simulations at section SC in Fig. 1.

Table 3. Mass of oxygen (kg) transported across section NC (above) during 5-day intervals for simulations conducted with different starting dates (d_0). The averaged dissolved oxygen concentration from 5-12 m in section NC for the different 5-day intervals in the simulations are shown below (g m^{-3}).

	5-day intervals in calculations									
	170-175	175-180	180-185	185-190	190-195	195-200	200-205	205-210	210-215	215-220
d_0	**Mass of oxygen (kg) transported across section NC**									
165	-160	-200	-658	**-2257**	-1553					
170		-122	-480	-2037	**-1571**	-632				
175			-249	-1386	-1342	**-564**	-668			
180				-722	-977	-460	**-639**	-1852		
185					-551	-337	-583	**-1652**	-558	
190						-167	-540	-1719	**-534**	-1507
	Averaged DO concentration at section NC (gm^{-3}) from 5-12 m									
165	0.11	0.38	0.68	**0.81**	0.98					
170		0.11	0.37	0.60	**0.81**	1.23				
175			0.12	0.35	0.59	**1.02**	1.17			
180				0.13	0.34	0.76	**0.93**	1.11		
185					0.13	0.47	0.67	**0.88**	1.13	
190						0.19	0.43	0.75	**1.01**	1.13

Table 4. Strong wind events in a 10-year data set collected in Atmore AGDM meteorological station (54.7802°N, -112.8248) located ≈ 24 km northwest from Amisk Lake. Those events are identified as periods of time of at least 6h in duration when the wind speed exceeds the 75 percentile of the 10-year hourly data set.

Month	Number of Events	Duration (h)	$w_{av}(ms^{-1})$	$w_{max}(ms^{-1})$	$P_{90}\ (ms^{-1})$
1	8	12.76	5.23	5.67	5.54
2	9	9.98	4.89	6.72	5.39
3	10	12.58	5.82	7.03	6.36
4	13	12.95	4.42	5.81	4.73
5	15	12.25	4.93	6.31	5.55
6	11	12.51	5.56	5.56	5.56
7	10	10.89	5.03	6.69	5.46
8	9	9.80	7.24	15.44	7.85
9	11	10.80	7.50	12.19	8.50
10	11	11.80	8.65	10.67	10.11
11	7	10.96	7.01	10.22	8.06
12	6	13.03	5.16	6.69	5.81
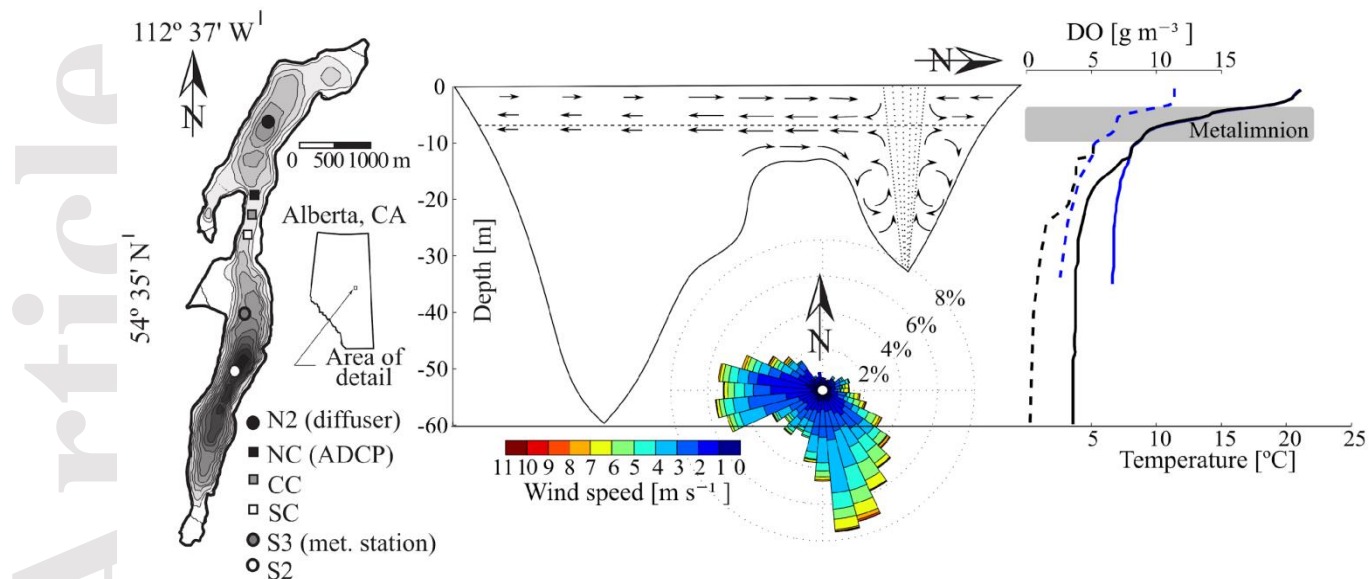
Figure 1. Bathymetry of Amisk Lake, Canada. Also shown are the sampling and measurement sites of Lawrence et al. (1997): sites S2 and N2 (temperature and dissolved oxygen profiles), S3 (meteorological station) and NC (ADCP). Schematic of possible circulation pattern driven by the oxygenation system (adapted from Lawrence et al., 1997). Temperature (solid line) and dissolved oxygen (broken line) profiles collected on Day 181, at sites S2 (black line) and N2 (blue line). Wind direction was predominant from the West and from the South and it is representative of a typical summertime forcing over Amisk Lake (Imam et al., 2013).
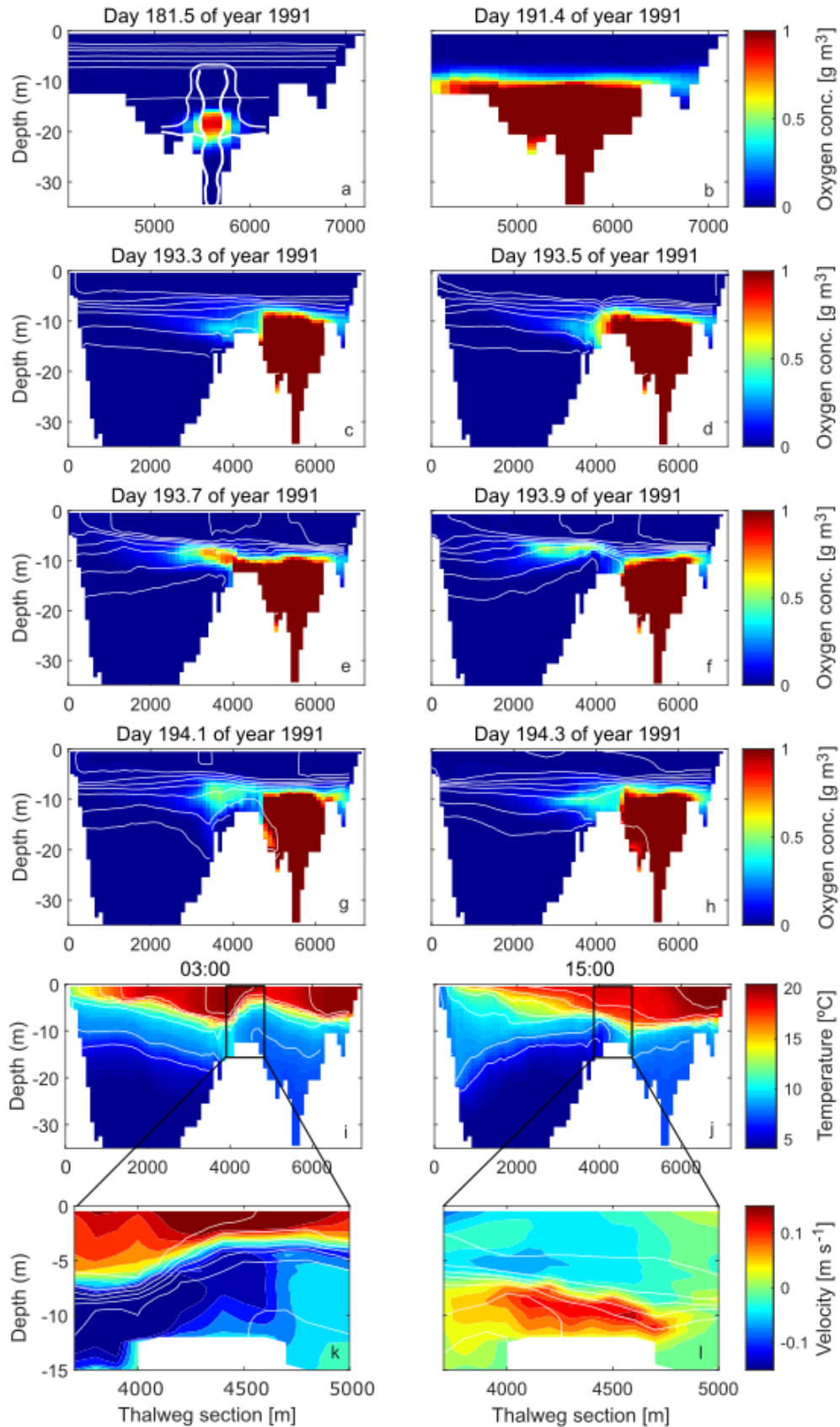
Figure 2. (**a-h**) Series of injected plume-DO concentration fields on a longitudinal section along the lake thalweg from the southern end of the lake to the northern end. (**a**) The detrainment plume DO in the N-basin is shown at the beginning of the injection. (**b**) The added oxygen replenished the hypolimnion in the N-basin before reaching the sill level. (**c-h**) Evolution of the added-DO concentration fields after a strong wind event on day 193. (**i-j**) Longitudinal sections of the temperature field and (**k-l**) close-up view of the velocity field along the channel that illustrate the response after 3 hours (**i**, **k**) and 15 hours (**j**, **l**) to a hypothetical 12-hour southerly wind event followed by a 12-hour period of calm. White lines in (**a-l**) show 2°C spacing isotherms.
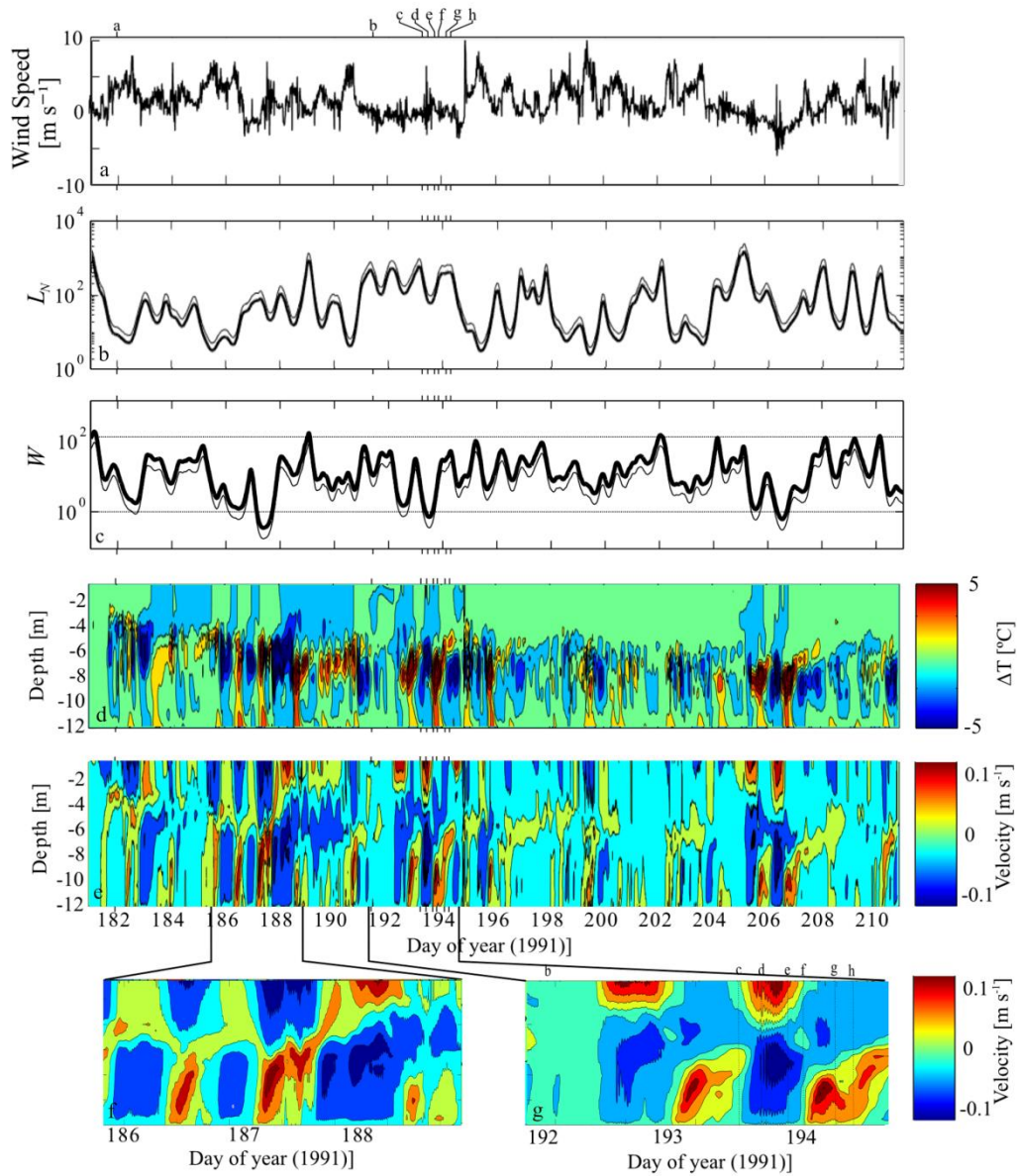
Figure 3. (**a**) Wind velocity along the thalweg (positive if directed towards the N-basin). (**b**) Lake (L_N), and (**c**) Wedderburn numbers (W) for the N- and S- basin, calculated using the temperature profiles collected at N1 (thick line) and S2 (thin line), respectively. (**d**) Modeled horizontal temperature gradients between sites NC and SC. (**e-g**) Modeled velocity field along the channel (positive if directed towards the N-basin) at site NC. Subplots (**f-g**) show a zoom-in of the velocity field during a wind event from (**f**) the north and from (**g**) the south. The labels (a-h) on the top of the figure match the time for the information displayed in Figs. 2a-h, respectively.
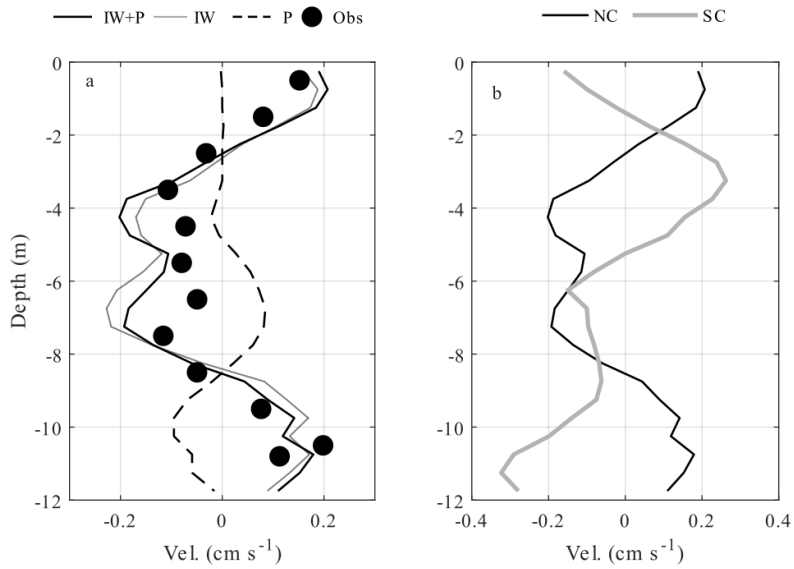
Figure 4. (a) Time-averaged (over the study period) velocity as observed at site NC (dots), representing the 'persistent, long-term average circulation' (Lawrence et al. 1997). Lines represent time- and space-(lateral) averaged velocity simulations at the cross-section NC for different scenarios. **(b)** Time-averaged simulated velocities at SC and NC for the reference scenario.
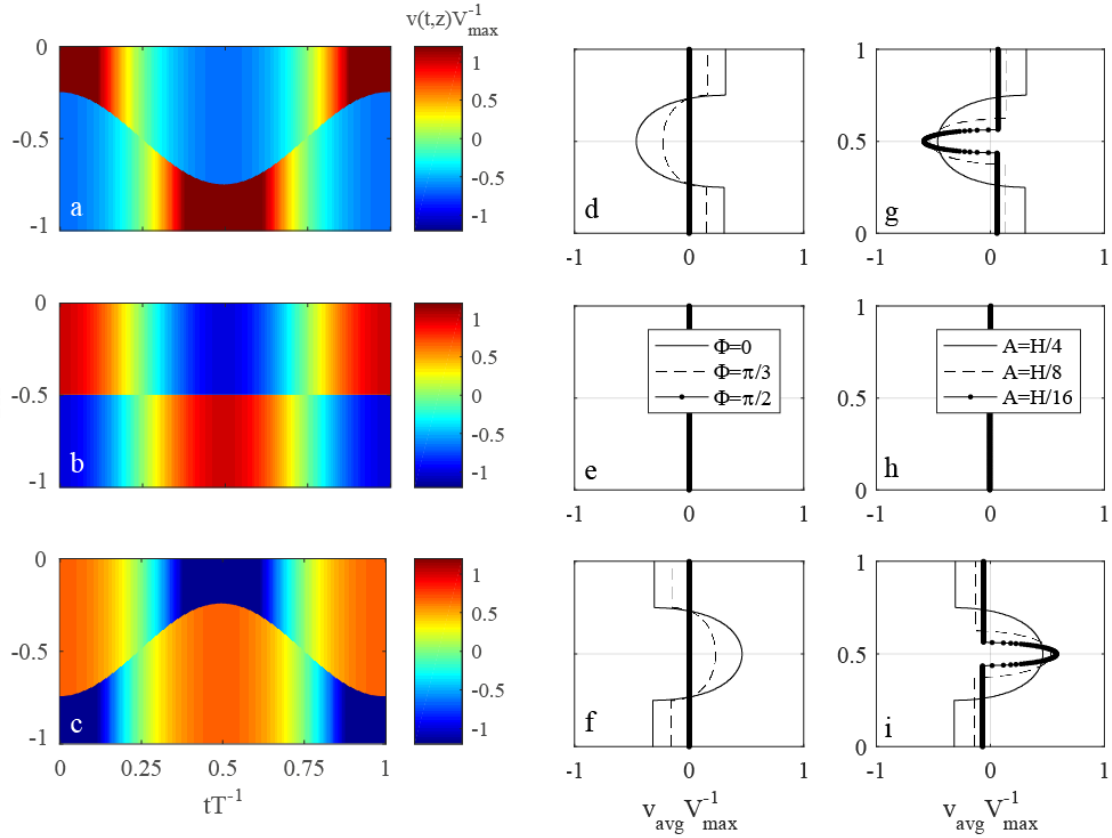
Figure 5. Simplified description of channel flow field. Instantaneous velocity profiles at (**a**) N- end of the channel, (**b**) center, and (**c**) S-end assuming in-phase ($\Phi = 0$) oscillatory flow rates and interfacial tilts. The velocity is positive northward. The subplots to the right represent the time-averaged velocity profiles during a complete period of oscillation at (d, g) N-end, (e, h) center and (f, i) S-end of the channel. On subplots (d) through (f) three averaged profiles are plotted for each site, assuming different lags Φ between flow rate and interfacial tilts ($\Phi = 0$, $\pi/2$ and $\pi/3$). On subplots (g) through (i), the three averaged profiles correspond to experiments conducted with different amplitudes of interfacial displacements and $\Phi = 0$.
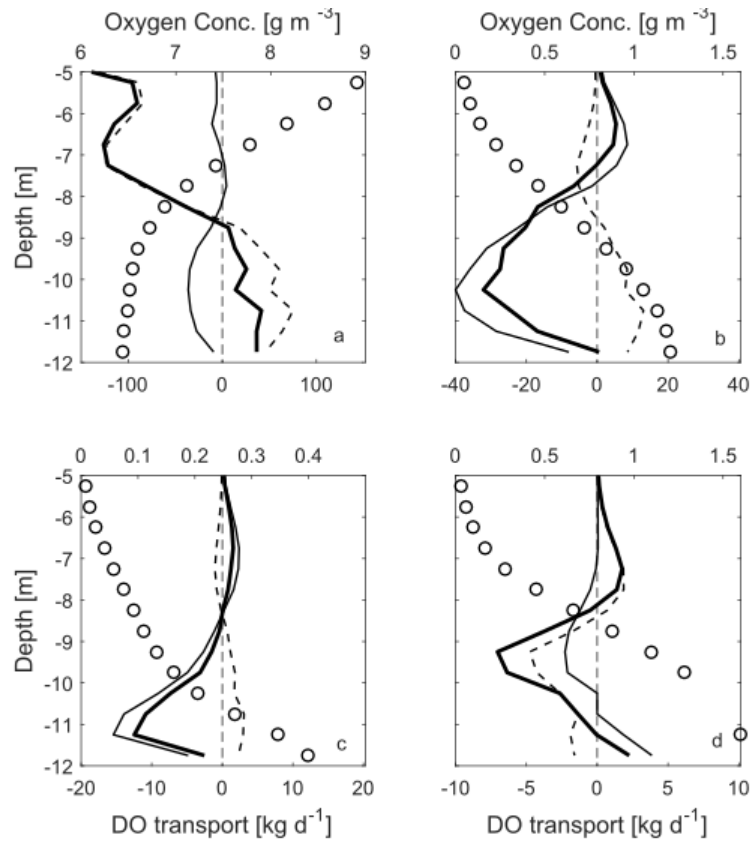
Figure 6. Average oxygen concentration O_{5-12} (upper axis) and oxygen load (lower axis) below the thermocline. The total oxygen load (thick continuous line) is decomposed into time-averaged transport component (dashed line) and fluctuating component (continuous thin line) for different forcing and tracer scenarios. Positive values indicate that oxygen transport is towards the N-basin. Estimates from simulations of (**a**) full DO and (**b**) injected plume- DO in the reference scenario. Also shown are the calculations made from the injected plume-DO simulations in (c) scenario IW and (**d**) scenario P. Note the scales used for the x-axis differ among subplots.
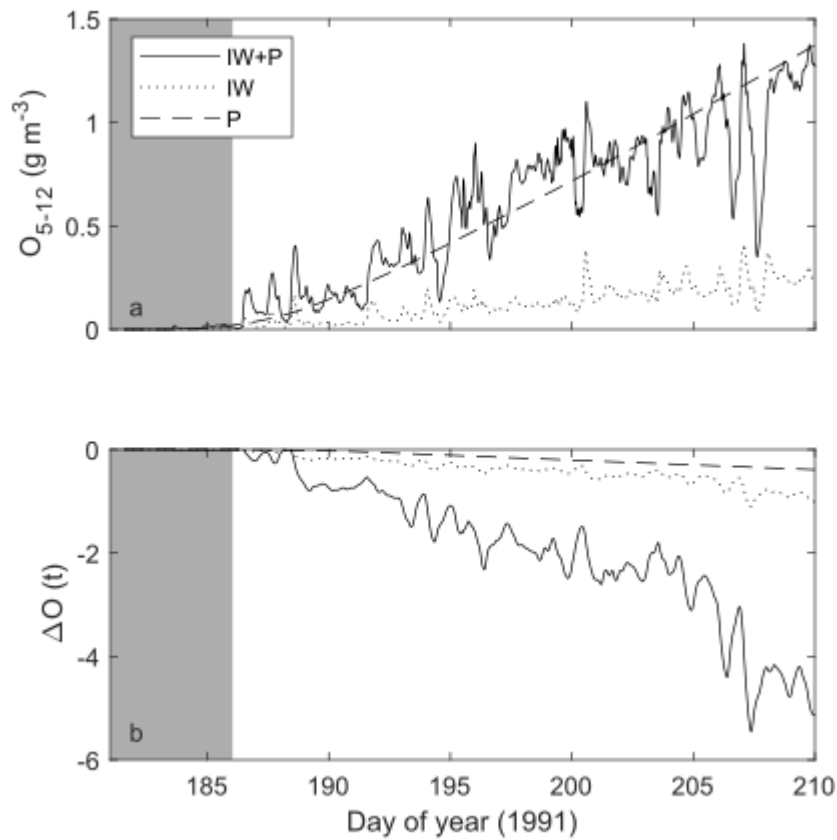
Figure 7. (a) Space-averaged injected oxygen concentration below the thermocline (5 m) at site NC. (b) Cumulative oxygen transport (tons) during the study period through section NC. The initial shadow region defines the filling period. The different lines represent results from different simulations.
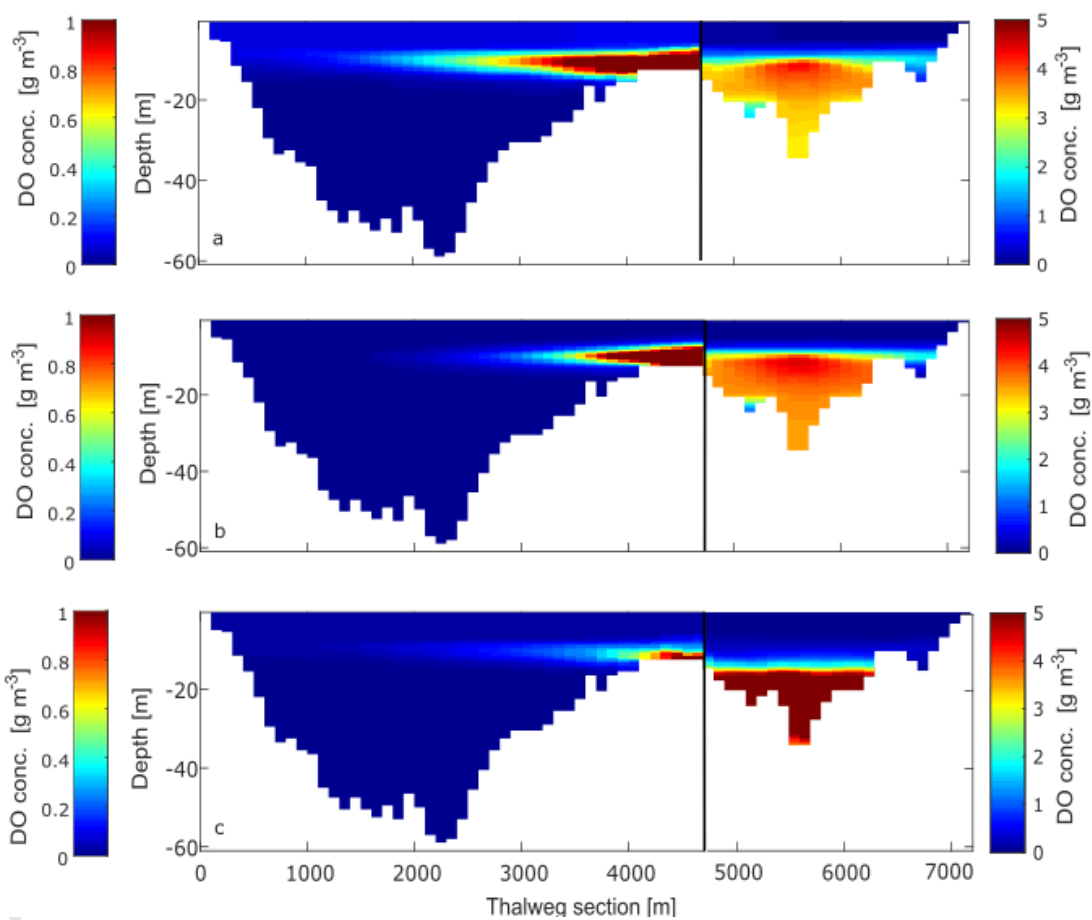
Figure 8. Distribution of the dissolved oxygen injected by the plume at the end of the study period along the lake thalweg in the (a) reference scenario, (b) scenario P, and (c) scenario IW. Two dissolved oxygen concentration scales are used in the figure to clarify the results.